Technical note: sea salt interference with black carbon quantification in snow samples using the Single Particle Soot Photometer

Marco Zanatta[1,a], Andreas Herber[1], Zsófia Jurányi[1], Oliver Eppers[2,3], Johannes Schneider[2], Joshua P. Schwarz[4]

[1] Alfred-Wegener-Institut, Helmholtz-Zentrum für Polar- und Meeresforschung (AWI), Bremerhaven, Germany
[2] Particle Chemistry Department, Max Planck Institute for Chemistry, Mainz, Germany
[3]Johannes Gutenberg University of Mainz, Institute for Atmospheric Physics, Mainz, Germany
[4]Chemical Sciences Laboratory, Earth System Research Laboratories, Boulder, CO, USA
[a]now at LISA, UMR CNRS 7583, Université Paris-Est-Créteil, Université de Paris, Institut Pierre Simon Laplace (IPSL), Créteil, France

Correspondence to: Andreas Herber (andreas.herber@awi.de)

Abstract

After aerosol deposition from the atmosphere, black carbon (BC) takes part in the snow albedo feedback contributing to modification of the Arctic radiative budget. With the initial goal of quantifying the concentration of BC in the Arctic snow and subsequent climatic impacts, snow samples were collected during the Polarstern expedition PASCAL (Polarstern cruise 106) in the sea-ice covered Fram Strait in early summer 2017. The refractory BC (rBC) content was then measured in the laboratory of the Alfred Wegener Institute with the single particle soot photometer (SP2). Based on the strong observational correlations between both rBC concentration and rBC diameter with snow salinity, we hypothesize a salt-induced matrix effect interfering with the SP2 analysis. This paper evaluates the impact of sea salt, based on the measurement of electrical conductivity (κ) in water samples, on rBC measurements made with a nebulizer-SP2 technique. Under realistic salinity conditions, laboratory experiments indicated a dramatic six-fold reduction in observed rBC concentration with increasing salinity. In the salinity conditions tested in the present work (salt concentration below 0.4 g l^{-1}) the impact of salt on the nebulization of water droplets might be negligible. However, the SP2 mass detection efficiency systematically decreased with increasing salinity, with the smaller rBC particles being preferentially undetected. The high concentration of suspended salt particles and the formation of thick salt coatings on

rBC cores caused problems to the SP2 analog-to-digital conversion of the signal and incandescence quenching, respectively. Changes to signal acquisition parameters and laser power of the SP2 improved the mass detection efficiency, which, nonetheless, stayed below unity. The present work provides evidence that a high concentration of sea salt undermines the quantification of rBC in snow performed with the SP2-nebulizer system described here. This interference has not been previously reported and might affect the future such analysis of rBC particles in snow collected, especially, over sea ice or coastal regions strongly affected by sea salt deposition.

1 Introduction

Black carbon (BC) aerosol, produced by incomplete combustion of biomass and fossil fuels, is transported from extensive mid-latitude source regions to the Arctic atmosphere (Schacht et al., 2019), where it influences the regional climate (Quinn et al., 2015). Once removed from the atmosphere, BC particles continue to affect the Arctic radiative budget by directly decreasing the snow albedo (Dou and Xiao, 2016) and promoting snow grain growth (Skiles and Painter, 2017). In turn, the acceleration of the melting rate leads to earlier exposure to the underlying surface. The overall process is usually called "snow albedo feedback", and might be considered among the strongest forcing mechanisms in the Arctic region (Hansen and Nazarenko, 2004; Flanner et al., 2007; Skiles et al., 2018).

Considering the climatic repercussions caused by BC in snow, the scientific community has been measuring the content of BC in snow across the Arctic for almost four decades (Clarke and Noone, 1985; Doherty et al., 2010; Dou and Xiao, 2016; Tørseth, 2019). Unfortunately, a standardized and universally accepted analytical technique for the measurement does not yet exist. Generally, the wide variety of analytical approaches to measure BC in snow can be divided into offline and online methods. Considering the offline approach, BC mass can be measured after melting and filtration of the snow sample via thermal-optical analysis (Hagler et al., 2007) or transmittance spectroscopy (Doherty et al., 2010). Alternatively, BC mass can be quantified, after the nebulization of the melted snow samples, with online techniques such as the photoacoustic technique (Schnaiter et al., 2019) or laser-induced incandescence technique (Schwarz et al., 2012).

In recent years the laser-induced incandescence technique, more specifically with the single particle soot photometer (SP2; Droplet Measurement Technologies, Longmont, CO, USA), was often used to quantify refractory black carbon particles (rBC; Petzold et al., 2013) concentrations in the snow and ice in various regions of the Arctic (Khan et al., 2017; Macdonald et al., 2017; Jacobi et al., 2019; Mori et al., 2019; Zhang et al., 2020). The rBC analytical procedure now generally includes three steps: 1) melting of the snow/ice sample, 2) nebulization with pneumatic concentric nebulizer equipped with a warming-cooling desolvating system (i.e. Marin-5 produced by Teledyne Technologies, Omaha, USA, and APEX-Q produced by Elemental Scientific Inc., Omaha, USA), 3) sampling the resulting aerosol with the SP2. During nebulization, the melted sample is usually transported to the nebulizer at a constant flow rate via a peristaltic pump. The liquid is then broken into small droplets and suspended in a nebulization chamber by means of a pneumatic concentric nebulizer. Once suspended, the solvent in the droplets is evaporated and removed with a warming cooling cycle. Several studies addressed the issue of reducing the losses of

rBC during the nebulization phases by controlling the liquid flow rate, gas flow rate, and pressure and temperature cycle (Lim et al., 2014; Wendl et al., 2014; Mori et al., 2016; Katich et al., 2017). Overall, up to 75% of rBC mass is suspended from the sample, transported through the nebulizer, and finally detected by the SP2 without the addition of surfactants (Lim et al., 2014; Mori et al., 2016). Due to the reduction of water density and viscosity, the doping with isopropyl alcohol increases the rBC mass nebulization efficiency to values close to unity (Katich et al., 2017). It must be considered that, despite corrections for the nebulization efficiency, the degree of comparability with more traditional techniques such as thermal-optical method and integrating sphere/integrating sandwich spectrophotometer is still variable (Schwarz et al., 2012; Lim et al., 2014; Mori et al., 2019).

In the Arctic region, many snow samples were collected in coastal regions and over sea ice (Tørseth, 2019) where the sea salt components often dominate the snow chemical composition, especially in summer in presence of open waters (Krnavek et al., 2012; Jacobi et al., 2019). This is particularly relevant over sea ice, where sea salt aerosol, suspended as sea spray, can be deposited at the snow surface, and capillary upward migration of sea salt from the sea ice can lead to high salt concentration at the bottom of the snowpack (Domine et al., 2004). Our surface snow samples, collected over the sea ice-covered Fram Strait in summer 2017 within the PASCAL experiment, were highly affected by salt deposition and showed a wide range of salinity. The presence of salt might have broad impacts on snow analysis, including via influence the nebulization of the sample, the analyte and solvent transport, and even the analytical signal of certain analytical techniques such as inductively coupled plasma atomic emission spectroscopy (e.g. L. Sharp, 1988; Luis Todolí et al., 2002; Burgener and Makonnen, 2020). Such effects are commonly called “matrix effects”. Until now, the potential interference of sea salt during the analysis of rBC particles with the SP2 has not been assessed.

Considering the high salinity of the snow samples collected in the Fram Strait, a series of laboratory experiments were conducted to quantify the impact of sea salt on nebulization and rBC detection with the SP2 instrument. This work aims to identify the importance of the salt matrix effect especially in the perspective of the MOSAiC (Multidisciplinary drifting Observatory for the Study of Arctic Climate, https://mosaic-expedition.org/) project, where hundreds of snow samples were collected, during the one-year-long drift over the sea ice, for the analysis of rBC in the snow with the SP2/nebulizer.

2 Technique

2.1 Snow sampling during the PASCAL expedition

The PASCAL expedition (Physical Feedbacks of Arctic Boundary Layer, Sea Ice, Cloud and Aerosol; Flores and Macke, 2018), organized within the framework of the AC3 project (Arctic Amplification: Climate Relevant Atmospheric and Surface Processes, and Feedback Mechanisms; Wendisch et al., 2018), was a shipborne field campaign on board of the *RV Polarstern*, the research icebreaker of the Alfred Wegener Institute (Bremerhaven, Germany). The 25 surface snow samples discussed here were collected on the sea ice during the drift phase, which occurred between 3 June and 16 June 2017 in the Fram Strait between 10.0°E - 11.5°E and 81.7°N - 82°N at a distance from open leads between 0.5 km and 1 km. These samples were collected in the first 5 cm of the snowpack and stored frozen at -20°C in

polypropylene tubes (Fisher Scientific GmbH, Schwerte, Germany) of 50 ml volume (typically 20-30 g water content) until analysis. For each snow sample, the physical properties of the corresponding snow layer were also measured. The specific surface area (SSA) was measured with the IceCube instrument (A2 Photonic Sensors, Grenoble, France), the snow density with a custom-made density cutter, and the snow temperature with a negative temperature coefficient one channel thermometer (model 101, Testo Ltd, Alton Hampshire, United Kingdom).

2.2 Instrumental setup during laboratory analysis

The experimental setup used for snow sample analysis is schematized in Figure 1. First, the snow samples were melted in a thermostatic bath at 25°C. Immediately after melting, the electrical conductivity (κ) of the liquid sample was measured with a portable conductivity meter (model: Cond 3110, WTW, Xylem Analytics, Weilheim, Germany) equipped with a 2-electrode conductivity cell (model KLE-325, WTW, Xylem Analytics, Weilheim, Germany). The probe was immersed in the sample and was rinsed with Milli-Q water before and after each measurement. Considering that the electrical conductivity generally increases by 2% per 1°C increase (Hayashi, 2004), we estimate that our κ measurements had a precision of 10%. The electrical conductivity of Milli-Q water never exceeded 1 μS cm^{-1} and was considerably lower than that of any snow sampled.

The sample was then fed via a peristaltic pump and through a liquid flow meter (model: Liquid Flow Meter SLI, Sensirion AG, Staefa, Switzerland) to a Marin-5 nebulizer (Teledyne Technologies, Omaha, USA). In the Marin-5, the liquid sample was aerosolized into an airflow by a concentric pneumatic nebulizer, and the resulting droplets were dehydrated by a heating-cooling cycle (110°C-5°C). Finally, the dry aerosol (relative humidity below 30%; Katich et al., 2017) was transported in tubings to the aerosol measuring instruments. The mass nebulization efficiency varied between 0.58 and 0.66 (see Section 3.3 for more details). A more detailed description of the Marin-5 nebulizer can be found in Mori et al. (2016). The liquid (70 μl min^{-1}) and air (1 l min^{-1}) flow rates were selected to maximize the suspension of rBC mass following Katich et al. (2017) and kept constant during all experiments. No surfactants were added to the snow samples or to the test suspensions/solutions. In this work, the aerosolized particles were directed to a Single Particle Soot Photometer (SP2; DMT, Longmont, USA), a Scanning Mobility Particle Sizer (SMPS; TSI; Shoreview, USA), and a single-particle mass spectrometer ALABAMA (Aircraft-based Laser Ablation Aerosol Mass Spectrometer; Brands et al., 2011; Köllner et al., 2017; Clemen et al., 2020). Our SP2 sampled the aerosol directly from the Marin-5 exhaust and provided number concentration (N_{rBC}), mass mixing ratio (M_{rBC}), and size distribution of rBC in the mass equivalent diameter (D_{rBC}) range of 70-1000 nm. D_{rBC} was calculated from the rBC-mass measured in individual particles using a void-free density of 1800 kg m^3 (Moteki and Kondo, 2010). The operating principles of the SP2 for atmospheric applications are given by Stephens et al. (2003), while assessments of the performance of the SP2 during snow sample analysis can be found in Lim et al., (2014), Mori et al. (2016) and Katich et al. (2017). The incandescence detectors of the SP2 were calibrated with mass-selected fullerene soot (FS; Alfa Aesar, LOT: W08A039) as described in Laborde et al. (2012b). The SMPS measured the number concentration (N) and size distribution between 14 nm and 680 nm mobility diameter (D_P). Multiple charges and diffusion losses were corrected with the aerosol instrument manager software issued by TSI. The ALABAMA was used to get additional information on the chemical

composition of single particles with diameters between approximately 110 and 5000 nm (Clemen et al., 2020). Different chemical species, identified using characteristic marker ions of the mass spectra, include: sodium chloride, magnesium, non-sea-salt nitrate, non-sea-salt sulfate, organic carbon, levoglucosan-dicarboxylic acids, elemental carbon. Both the SMPS and ALABAMA sampling line were diluted with air by a factor 10.

Transport losses of aerosol particles were calculated using the Particle Loss Calculator software, which treats aerosol diffusion and sedimentation as well as turbulent inertial deposition and inertial deposition in bends and contractions of tubing (von der Weiden et al., 2009). The software was developed at the Max Planck Institute for Chemistry of Mainz (Germany) and is available for download at https://www.mpic.de/4230607/particle-loss-calculator-plc (last accessed 08 April 2021).

3 Results

3.1 Surface snow properties in the Fram Strait

3.1.1 Snow physical properties

Warm conditions were encountered during the sampling campaign, with the air temperature increasing from approximately -4°C at the beginning of the campaign to approximately -1°C (with one-minute average values up to 2°C) at the end of sampling. As a consequence of temperature increase, the snow specific surface area (SSA) decreased from 70 m^2 kg^{-1} to 5 m^2 $kg^{-1,}$ and snow density increased from 280 kg m^{-3} to 350 kg m^{-3}. The electrical conductivity of surface snow decreased from values above 1000 μS cm^{-1} to κ values below 10 μS cm^{-1} towards the end of the campaign. The decrease of SSA and increase of snow density during the drift phase of the PASCAL expedition indicates the occurrence of melt-refreeze cycles (Haas et al., 2001; Massom et al., 2001; Domine et al., 2007), and the downward migration of soluble salts with percolating water explains the decrease of κ (Domine et al., 2004; Doherty et al., 2013). Considering the wide variability of electrical conductivity, the dataset was organized into 5 salinity classes (Sn). The samples with the lowest conductivity (κ ≈ 5-10 μS cm^{-1}) accounted for 38% of total samples and were mainly collected after the melting onset and grouped into S1. S2 includes the samples collected at the snowmelt which showed κ values between approximately 20-30 μS cm^{-1} and accounted for 17% of the samples. The samples characterized by a κ value above 200 μS cm^{-1} and below 2000 μS cm^{-1} represented 46% of the total number of the collected probes and were organized into three different salinity classes (S3, S4, S5). The most saline snow sample (κ = 3600 μS cm^{-1}) was excluded from further analysis. The mean and boundaries of κ values defining the five salinity classes are listed in Table 1.

3.1.2 Relationship between salinity of snow samples and particle aerosolization

Here we investigate the potential relationship between electrical conductivity, which is used here as a proxy for salinity, and the aerosolization of particles. Note that N and N_{rBC} are presented in this section without correction for the nebulization efficiency of the Marin-5 nebulizer.

Under fixed nebulization conditions (constant liquid sample flow and gas flow), a large number of particles (droplet residues) were suspended by the nebulization process. N increased with the electrical conductivity of the sample from $6.1*10^5$ cm^{-3} in low conductivity samples (κ < 10 μS cm^{-1}) to $1.5*10^6$ cm^{-}

^{3} for samples showing conductivity values above 1000 μs cm^{-1} (Figure 2a, Table 1). A similar trend was recently observed by Rösch and Cziczo (2020). The correlation of N with κ suggests that most of the aerosolized particles is composed of sea salt, which is expected to be the major solute in seawater. As indicated in Table 1, the size of the aerosolized particles (geometric mean of the number size distribution; GD_P) increased with κ from 27 nm (S1, κ < 10 μS cm^{-1}) to 89 nm (S5, κ>1000 μS cm^{-1}). The GD_P – κ relationship and the absence of multiple modes in the aerosol size distribution (Figure S1) support the assumption of sea salt controlling the aerosol composition. The increase of particle diameter with the liquid concentration of soluble inorganic salts was already observed (Clifford et al., 1993) and was found to be mainly caused by the higher concentration of salt in the primary aerosolized droplets. Additionally, particle growth caused by coalescence and promoted by the high number concentration of aerosolized particles might also contribute to the diameter shift (Olivares and Houk, 1986). The shift of the size distribution mode into the size detection range of the SMPS might also contribute to the N-κ positive correlation shown in Figure 2a.

The ALABAMA measurements confirmed the predominant presence of seawater components such as sodium chloride (NaCl) and magnesium (Mg) over other chemical species shown in Figure 3. The particle fraction (*PF*) of NaCl-containing particles increased from roughly 30 % for the lowest salinity class to 60-80 % of all analyzed particles for S2, S3, S4, and S5. A similar increase was observed for Mg-containing particles. Other particle species, e.g. non-sea-salt (nss) nitrate and sulfate, were only relatively abundant in samples with low conductivity. For salinity class S4, the fraction of NaCl- and Mg-containing particles is significantly lower compared to other classes with κ>10 μS cm^{-1} which is due to one sample of S4 containing more of the other particle species.

SP2 measurements indicated a monotonic decrease of N_{rBC} with conductivity (Figure 2b, Table 1), opposite to N. Considering only the salinity classes, the rBC number concentration decreased from approximately 70 cm^{-3} in S1 to 1.7 cm^{-3} in S5. Additionally, the number size distribution of detected rBC particles showed a shift to larger diameters as a function of salinity (Figure S1b). The resulting rBC geometric mean diameter calculated from the number size distribution ($GD_{rBC\text{-}N}$), increased from approximately 90 to 120 nm from S1 to S5 (Table 1). The detected rBC mass mixing ratio (M_{rBC}) monotonically decreased with κ from 8.05 ng g^{-1} in S1 to 0.27 ng g^{-1} in S5 (Figure 2c). Although M_{rBC} concentrations have already been observed in different locations and seasons across the Arctic (Sinha P. R. et al., 2017; Jacobi et al., 2019; Mori et al., 2019, 2020) and might be partially explained by BC redistribution during melting (Doherty et al., 2013); here the abrupt (factor 12) and sudden (48 hours) increase, observed between S3 and S1, of M_{rBC} at the snow surface was never observed in the Arctic region and is not believed to be physical. The M_{rBC} values presented here are corrected only for the mass nebulization efficiency (see more detail in Section 3.3). Similar to $GD_{rBC\text{-}N}$, the rBC geometric mean diameter calculated from the mass size distribution ($GD_{rBC\text{-}M}$), increased from 225 nm to 257 nm from S1 to S5 (Table 1). Considering that the melt-freeze cycle promotes agglomeration of BC particles (Schwarz et al., 2012; Kinase et al., 2020), the decrease of $GD_{rBC\text{-}M}$ at the melt onset (S1-S2) was unexpected. The respective rBC mass size distributions are shown in Figure S1c.

These results make it clear that rBC-containing particles represent the small minority of the aerosol population nebulized from the snow samples. In fact, the number fraction of detected rBC particles (F_{rBC}) decreased with salinity from 1.1*10^{-2} % in S1 to 1.1*10^{-4} % in S5 (Table 1). Moreover, elemental carbon (EC-) containing particles were found in less than 1% of all analyzed particles by ALABAMA (Figure

3). Hence, considering the remarkable concentration of total particles, the minor fraction of rBC particles, the sudden decrease of M_{rBC} with conductivity, and the unexpected diameter decrease at the melt onset, laboratory experiments were designed to reproduce the salinity conditions of PASCAL snow samples to investigate the potential interference mechanisms of salt on rBC detection by the SP2. We find that the rBC properties presented in this section were prone to high error and are not be representative of natural processes only. This is particularly relevant for the saline samples belonging to S3-S5.

3.2 Reproducing realistic snow samples conditions in laboratory experiments

The laboratory experiments aimed to reproduce BC snow concentrations representative of generic Arctic conditions, and the specific salinity conditions representative of PASCAL snow samples. It is important to note that the salt concentrations explored in the present work do not represent realistic conditions encountered in continental or mountain regions where sea salt aerosol deposition is not dominant. The ability to reproduce such conditions and practical limitations are presented in the following.

3.2.1 Sample preparation

Fullerene soot (FS; Alfa Aesar, LOT: W08A039) was used as a proxy for ambient black carbon. FS is a well-characterized standard for SP2 calibration (Gysel et al., 2011; Laborde et al., 2012a) and is accepted as the reference standard for ambient black carbon (Moteki and Kondo, 2010; Baumgardner et al., 2012). Three different inorganic salts were chosen to replicate the conductivity array of the snow samples: sodium chloride (NaCl, Fluka), potassium chloride (KCl, Fluka), and ammonium sulfate ($(NH_4)_2SO_4$, Sigma Aldrich).

The proportionality between electrical conductivity and the mass concentration of the salts was assessed (Figure S2). All the saline solutions showed a linear relationship between conductivity and mass concentration, with a high correlation coefficient ($r^2>0.98$) and no dependence on salt composition. We have chosen the concentration range of the dissolved salt to be between approximately 3 mg l^{-1} and 870 mg l^{-1} to match the range of salinity values between the lowest and the highest boundaries of the S1-S5 classes. As in the case of snow samples, the number concentration of aerosolized particles (measured by the SMPS in the size range of 14-680 nm) increased with salinity (Figure 4) from approximately $6*10^5$ cm^{-3} at S1 ($\kappa \approx 7$ μS cm^{-1}) to approximately $1.7*10^6$ cm^{-3} at S5 ($\kappa \approx 1450$ μS cm^{-1}). The number concentration of particles produced by nebulization of saline solutions is similar to that of the snow samples, within 10% for the S1-S4 classes and within 15% for S5. The increase of particle diameter with conductivity observed in the snow samples was also closely replicated by the saline solutions (Figure 5). The increase of concentration and diameter of total suspended particles with salinity observed in the snow samples was successfully reproduced with salt standards, justifying the use of inorganic salts to simulate the snow saline conditions. Due to the similarity of results between the different salts, and to the fact that NaCl was the major component of PASCAL samples (Figure 3), NaCl was chosen as the reference salt for all the experiments presented in the rest of the study.

3.2.2 Salt induced limitations to SP2 operation

Although ambient salinity conditions were successfully reproduced, the SP2 was not able to operate for stably under the most concentrated salt conditions. For the ambient samples, the SP2 was only exposed to the highest concentrations intermittently, and for short times. However, for more focused laboratory conditions here, the range of BC and salt concentration the SP2 was exposed to was limited, compared with ambient conditions, to ensure stable SP2 operation.

3.2.2.1 SP2 laser beam shadowing

During the snow-sample analysis, the large light extinction of the dense aerosol produced from one extremely saline sample (κ = 3600 μS cm^{-1}) caused a marked but temporary decrease of the YAG power (approximately 50% reduction). The laser power completely and immediately recovered after switching to clean air sampling. Despite this extreme event, in the salinity range of our snow samples (κ< 1652 μS cm^{-1}), the YAG power decreased only 2% with increasing salinity. This effect on net laser intensity in the cavity might, thus, be important for extremely saline solutions, but is negligible for solution or samples with κ below 1500 μS cm^{-1} at the rates we nebulized the liquid.

3.2.2.2 SP2 flow system

The prolonged sampling of rich saline solution affected the flow system of the SP2. The sampling time needed to acquire a minimum of 30 000 recorded particles substantially increased with decreasing FS concentration (Figure S3). The prolonged nebulization (longer than 30 minutes) of 1 μg l^{-1} and 5 μg l^{-1} FS suspension with electrical conductivity equal and above 600 μs cm^{-1} led to the accumulation of salt in the SP2 aerosol jet tubing. This finally formed a solid obstruction and caused the decreased sampling flow rate and the pressure at the detection chamber. To remove the salt obstruction, the full jet assembly was disconnected from the SP2, the clogged section of the metal tubing was first soaked in Milli-Q water, sonicated for a few seconds, and dried with compressed air. The formation of the salt obstruction and its removal altered the flow rate sensor accuracy and could have modified the alignment of the sample aerosol with the laser. Due to the unknown degree of uncertainty, the first set of experiments at different FS concentration are not shown. Moreover, to shorten the duration of the measurements and minimize the risk of clogging, all of the following experiments were performed with FS suspensions with a concentration of 10 μg l^{-1}. Although previous SP2-based studies reported lower rBC mixing ratios in the Arctic (Sinha P. R. et al., 2017; Jacobi et al., 2019; Mori et al., 2019, 2020), this value is fairly comparable to the M_{rBC} observed in the PASCAL samples for the less saline samples (8.05 ng g^{-1}, Table 1). To further reduce chances for clogging, the upper limit of FS suspension's κ was set to 800 μS cm^{-1} (approximately 0.4 g l^{-1} of NaCl). Considering our inability to reproduce the most extreme sample conditions (low BC and high salt concentration), the SP2 results acquired during the analysis of S5 samples are affected by unknown bias. However, it is unlikely that lower BC concentration contributes to this additional uncertainty.

3.3 Salt impact on the rBC mass quantification by the SP2

In this section, we investigate the possible impact of salt on the SP2 rBC quantification using the laboratory-generated snow sample proxies. When nebulizing liquid samples, the overall mass quantification efficiency of rBC (ε) can be calculated as the mass of rBC pumped into the nebulizer per

unit time divided by the mass of rBC coming out of the nebulizer in aerosol form and detected by the SP2 per unit time (Katich et al., 2017):

$$\boldsymbol{\varepsilon = \frac{M_{rBC-SP2}}{M_{rBC-smp}} * \frac{F_{Gas}}{F_{Liq}}} \quad (1)$$

Where $M_{\text{rBC-SP2}}$ is the mass concentration of rBC particles quantified by the SP2 and $M_{\text{rBC-smp}}$ is the mass concentration of rBC particles in the liquid sample. F_{Gas} is the gas flow rate applied to the nebulizer and F_{Liq} is the liquid flow rate of the sample pumped into the nebulizer. ε may be decomposed in three distinct contributions: the mass nebulization efficiency (ε_{Neb}), the transport efficiency (ε_{Trn}) and the mass detection efficiency of the SP2 (ε_{SP2}). ε_{Neb} is the mass of rBC pumped into the nebulizer per unit time divided by the mass of rBC coming out of the nebulizer in aerosol form per unit time. Hence, ε_{Neb} depends on the suspension efficiency of the liquid sample in liquid droplets and on the transport efficiency of the wet and dry aerosol within the nebulizer. ε_{Trn} is the ratio of the mass of rBC pumped out the nebulizer per unit time to the mass of rBC reaching the SP2 sampling inlet per unit time. ε_{Trn} is controlled by diffusion, impaction, and sedimentation losses, and depends on flow rate, particle size and the length, orientation, and bends of the sampling line. ε_{SP2} is the mass of rBC in the aerosol form being introduced to the SP2 laser per unit time divided by the mass of rBC in aerosol form reported by the SP2 per unit of time. Considering typical atmospheric SP2 operation, ε_{SP2} depends on the size distribution of rBC particles, the presence of other absorbing-refractory atmospheric components, and SP2 size detection range configuration (Schwarz et al., 2010). The ideal, but unrealistic, ε of 1 indicates that 100% of rBC particles contained in the liquid sample are nebulized, transported, and finally detected by the SP2. In reality, the ε values obtained for various soot standards suspended in pure water and nebulized with the Marin-5 nebulizer vary between 0.5 and 0.6 (Mori et al., 2016; Katich et al., 2017), while ε of 0.75 was calculated by Lim et al. (2014) using an APEX-Q nebulizer. The ε calculated in the present work for non-saline suspensions at different FS mass concentrations varied between 0.57 and 0.66. Our results are in good agreement with the previous studies, indicating good reproducibility of nebulization conditions during the laboratory experiments. It must be considered that past studies always assumed 100% ε_{SP2} and ε_{Trn} for rBC particles falling in the size detection range of the SP2. Therefore, ε (calculated exactly as in this study according to Equation (1) was usually addressed as nebulization efficiency. In this study, ε decreased monotonically down to values between 0.33 and 0.21 for the most saline FS suspensions (κ = 800 cm^{-1}). This decrease clearly indicated a salt induced bias on the mass quantification efficiency. Hence, the assumption of a 100% ε_{SP2} and ε_{Trn} might not be realistic for saline samples. The potential impact of salt presence on the nebulization and transport efficiency, and on the SP2 detection efficiency will be addressed in the following subsections.

3.3.1 Nebulization and transport efficiency

Inorganic salt can alter water physical properties such as viscosity and surface tension, modifying the size distribution of droplets produced in the spray chamber and affecting the nebulization efficiency of various analytes (Todolí et al., 2002). High surface tension and viscosity cause an increase in the mean diameter of the liquid droplets suspended by pneumatic nebulizers, decreasing their transport efficiency (L. Sharp,

1988). NaCl concentrations above 1 g l^{-1} cause a significant increase in the droplet diameter (Clifford et al., 1993) and a decrease in transport efficiency (Sötebier et al., 2016). However, previous studies on pneumatic nebulizers (Dubuisson et al., 1998; Cano et al., 2002) indicated that the salt matrix effect on the liquid droplet diameter and transport at concentrations below 1 g l^{-1} is negligible. Note that, as summarized by Todolí et al. (2002), several studies have reported different or contradictory results on the impact of matrix effect during the nebulization process with pneumatic nebulizers. Thus, the understanding of processes causing diameter increase and efficiency decrease remains uncertain. The viscosity and surface tension of our NaCl solutions was extrapolated from Lide (1995) and Ozdemir et al. (2009), respectively. 0.8 g l^{-1} of NaCl, representative of S5 samples (κ = 1400 µS cm^{-1}), causes a small increase of both viscosity (+0.08%) and surface tension (+0.03%) compared to pure water. Our calculations and the results of Dubuisson et al. (1998) and Cano et al. (2002) indicate a negligible change of water properties and thus nebulization efficiency for the salinity levels tested in the laboratory experiments (κ below 800 µS cm^{-1}, NaCl concentration below 0.4 g l^{-1}). Considering the dominant presence of NaCl in the snow samples (Figure 3), our calculations also represent the salt-influenced snow samples. To support our calculations, the mass quantification efficiency was calculated for NaCl solutions (ε_{NaCl}) at different salt concentration from SMPS measurements (14 nm < D_p < 680 nm). The aerosolized mass concentration of the NaCl was calculated assuming spherical particles with a density of 2170 kg m^{-3} (manufacturer data). Considering the factor 10 dilution, which enabled SMPS operation below the highest limit of the detection, and the low RH (<30%), we assumed a SMPS detection efficiency of 100% in the 14-680 nm diameter range. Thus, ε_{NaCl} should solely be affected by nebulization efficiency. ε_{NaCl} remained very stable (range of 0.57-0.58) from low (κ = 25 µS cm^{-1}) to high (κ = 800 µS cm^{-1}) salinity. In turn, this suggests that the nebulization efficiency of rBC particles is independent of salinity (salt concentration below 4 g l^{-1} or electrical conductivity below 800 µS cm^{-1}.

The transport losses were estimated for the SP2 sampling line, which was 30 cm long (distance from the Marin-5 exhaust) and composed of two different sections. The first section was 24 cm long with an internal diameter of 4.82 mm, an airflow rate of 1 L min^{-1}, and carried flow to SP2, SMPS, and ALABAMA. After a two-way flow splitter with a "Y" joint (model 1100; Brechtel, Hayward, USA), the SP2-specific sampling line was 6 cm long with an internal diameter of 1.8 mm, and an airflow rate of 0.12 L min^{-1}. No sharp bends or additional flow splitters were present along the second section. We assumed spherical particles with a void-free density of 1800 kg m^{-3} (Moteki and Kondo, 2010). Losses of 2-5% and 2-16% were calculated for smaller (10-40 nm) and larger (1-5 µm) particles, respectively. The particle losses in the SP2 detection range (70-1000 nm of diameter) were estimated to remain well below 2%; hence not taken into account in forthcoming calculations.

3.3.2 SP2 detection efficiency

In this section, we will investigate the consequences of high number particle density transiting the SP2 laser beam on its data acquisition system at different acquisition settings. Additionally, the potential quenching of incandescence caused by the presence of thick salt coatings on rBC cores will be addressed. ε_{SP2} is the ratio between reported M_{rBC} of the NaCl-doped suspensions at a certain conductivity (κ>0 µS cm^{-1}; κ_x) and the M_{rBC} of the non-saline reference suspension ($\kappa \approx 0$ µS cm^{-1}; κ_0) as:

$$\varepsilon_{SP2}(\kappa_x) = \frac{M_{rBC}(\kappa_x)}{M_{rBC}(\kappa_0)} \quad (2)$$

A size-dependent ε_{SP2} is the ratio of the mass size distribution at a specific conductivity (κ_x) over the mass size distribution of non-saline suspensions (κ_0) at a certain rBC diameter (D_{rBC}):

$$\varepsilon_{SP2}(\kappa_x, D_{rBC}) = \frac{dM_{rBC}(\kappa_x, D_{rBC})}{dM_{rBC}(\kappa_0, D_{rBC})} \quad (3)$$

where dM_{rBC} represents the mass concentration of rBC particles contained in each diameter bin of the rBC mass size distribution.

3.3.2.1 Sensitivity of data acquisition to sample salinity

The frequency of recorded scattering events increased up to 17500 counts per second for saline solutions with 250 μS cm^{-1} electrical conductivity (Figure S4). Considering the high frequency of simultaneous events (multiple particles passing through the laser beam during one acquisition period), this number is most likely lower than the rate of particles entering the instrument. Operating the SP2 at this overloaded condition might lead to data loss caused by the limitation of the analogue to digital converter and computational power of the instrument's PC. This is possibly responsible for the observed exponential decrease of the frequency of detected scattering events for saline solutions with κ values above 250 μS cm^{-1}. Simultaneous particles and trigger hysteresis (used to reduce some types of data artifacts in the SP2) issues do not only reduce the acquisition of scattering events but also cause the decrease of detected incandescence events' frequency (Figure S4). Considering the low concentration of rBC particles with the high concentration of non-rBC particles, the acquisition settings become extremely important to avoid non-detection of individual incandescence signals. The importance of triggering choices was, hence, tested with 10 μg l^{-1} FS concentration and increasing NaCl concentration (conductivity range of 0 - 800 μS cm^{-1}). The mass detection efficiency was then measured with either the signal acquisition triggering off only the high-gain scattering channel ($\varepsilon_{SP2\text{-}Tsc}$) or only off the broad-band high-gain incandescence channel ($\varepsilon_{SP2\text{-}Tin}$).

First, the result obtained by triggering on the scattering detector (the typical setup when operating the SP2 for atmospheric observations) will be discussed. $\varepsilon_{SP2\text{-}Tsc}$ steadily decreased with conductivity to 0.34 at 800 μS cm^{-1}, while the rBC mean diameter increased from 180 at 0 μS cm^{-1} nm to 207 nm at 800 μS cm^{-1} (Figure 6). The increasing rBC mean diameter indicates size dependency in $\varepsilon_{SP2\text{-}Tsc}$ (see rBC size distribution in Figure S5). Indeed, $\varepsilon_{SP2\text{-}Tsc}$ systematically increased with D_{rBC} across the entire salinity range tested in the present study (Figure 7a). At lower conductivity ($\kappa < 200$ μS cm^{-1}), $\varepsilon_{SP2\text{-}Tsc}$ increased from approximately 0.4-0.6 for rBC components smaller than 100 nm to values above 0.7 for rBC components larger than 200 nm. The difference of $\varepsilon_{SP2\text{-}Tsc}$ across the rBC size distribution was remarkable at higher conductivity ($\kappa > 600$ μS cm^{-1}), where $\varepsilon_{SP2\text{-}Tsc}$ increased from 0.1-0.2 for D_{rBC} below 100 nm to 0.4-0.6 for D_{rBC} above 300 nm. It is thus evident that not only the mass concentration but also the size distribution of rBC might be strongly biased when the standard atmospheric configuration of the SP2 is implemented measurements of liquids with significant salt content. Below 200 μS cm^{-1}, no significant

difference could be identified between $\varepsilon_{SP2\text{-}Tsc}$ and $\varepsilon_{SP2\text{-}Tin}$. This result indicates that triggering settings are not crucial for snow samples with up to 0.1 g l^{-1} water salt content, in the absence of contaminants. Triggering only off the incandescence signal reported 20-50% more rBC mass compared to triggering only off the scattering signal at higher salinity (κ>200 µS cm^{-1}). Similar to $\varepsilon_{SP2\text{-}Tsc}$, $\varepsilon_{SP2\text{-}Tin}$ showed an increasing trend with D_{rBC} at all considered electrical conductivities (Figure 7b). Note here that for D_{rBC} larger than 400 nm, low rBC concentration resulted in statistical uncertainty that caused unrealistic εSP2 values above 1. These results indicate that the triggering setting does not appear to substantially modify the size dependency of the SP2 detection efficiency. Nevertheless, the use of the scattering trigger should be avoided in future studies when analyzing rBC in snow samples. Diluting these saline samples to achieve only single particles per detection in the SP2 (Katich et al., 2017), would likely reduce the detection problem even for samples with κ above 200 µS cm^{-1} (NaCl concentration above 0.1 g l^{-1}).

3.3.2.2 Incandescence quenching

Very thick coatings encapsulating rBC cores might not permit the SP2 laser to penetrate the coating, warm the rBC core, evaporate the coating, and finally allow correct detection by bringing the rBC to vaporization temperature. This phenomenon will be called incandescence quenching. During nebulization of saline samples, the salt contained in each droplet will remain on the rBC component after the water is evaporated, and create thick coatings encapsulating the rBC.

As a rough estimation, we calculated the theoretical coating thickness and coating-rBC mass ratio of spherical rBC cores having a diameter of 100 nm, 200 nm, 300 nm, 400 nm, 500 nm as a function of salinity. We assumed the presence of a single rBC core per droplet, a concentric core-shell geometry and NaCl density of 2170 kg m^{-3}. No direct measurements of the droplet size distribution are available for the Marine-5 nebulizer, but Mori et al. (2016) calculated a hypothetical droplet diameter of 2.5 µm based on the size distribution of total particles nebulized with the Marin-5 from an ammonium sulphate solution at a known concentration of 13.4 mg l^{-1}. By using the same equation, we calculated a droplet diameter of approximately 20 µm for a NaCl solution at a similar concentration of 13.1 mg l^{-1} (κ=25 µS cm^{-1}, representative of S2). Considering the marked difference with the result of Mori et al. (2016), most probably due to an oversimplification of the nebulization process, we assumed a droplet diameter of 8 µm. This value represents the peak of the primary droplet number size distribution suspended by various concentric pneumatic nebulizers working with a gas flow rate of 1 l min^{-1} and a liquid flow range of 11-20 µl min^{-1} (Burgener and Makonnen, 2020). The calculated coating thickness and coating-rBC mass ratio can be found in Table S1 and Table S2, respectively. The thickest coatings are expected for the smallest rBC cores (100 nm of diameter) with values increasing from 47 nm at 50 µS cm^{-1} to 182 nm at 800 µS cm^{-1}. The coating thickness of the largest cores considered here (500 nm) was significantly smaller, having values below 55 nm for the considered NaCl concentration. Similarly, the mass fraction of coating material decreased with the rBC core diameter. Laboratory experiments showed that relatively thin coatings (coating-rBC mass ratio below 3.5) do not have any significant negative impact on the SP2 detection efficiency (Schwarz et al., 2010). According to the coating calculation presented above (droplet diameter 8 µm), a coating-rBC mass ratio above 3.5 is expected for rBC particles with a diameter below 300 nm. For 100 nm particles, the coating-rBC mass ratio was calculated to exceed a value of 7 at a salinity of 50 µS cm^{-1}. The mass of salt associated with each core is assumed to be constant, but the absorption cross-section scales approximately linearly with the mass of the rBC core, as the cube of the

rBC diameter. Hence the potential for salt to quench incandescence is highest for the smallest rBC cores. This phenomenon could explain the measured ε_{SP2} values' diameter dependence shown in Figure 7. Considering our calculation, and the size-dependent detection results obtained by Schwarz et al. (2010), incandescence quenching is likely particularly important for the smallest rBC particles. It must be noted that the calculated coating thickness and mass ratio are only a rough assumption since its value strongly depends on the size and mass of the nebulized droplets. Assuming 12 µm and 5 µm droplet diameter (upper and lower mode of the droplet size distribution shown in Burgener and Makonnen, 2020) the coating-rBC mass ratio increases by, approximately, a factor of 10.

To further investigate the potential quenching effect of salt, FS suspensions (FS concentration of 10 µg l^{-1}) with increasing NaCl concentrations were nebulized and analyzed with the SP2 operating at maximum YAG-laser power and signal acquisition triggered only with the incandescence signal. High YAG-laser power is expected to speed the vaporization of thicker coatings and to increase the mass detection efficiency of rBC (Schwarz et al., 2010). During standard operating conditions, and for the previous results, the pump laser was operated below peak power. For the following experiments, the laser power was increased to its upper limit (leading to an increase of the YAG-laser power output from 5.2 V to 6 V. The mass detection efficiency and its size distribution, here called $\varepsilon_{SP2\text{-}Ymax}$, were calculated according to Equation 1 and Equation 2, respectively. $\varepsilon_{SP2\text{-}Ymax}$ decreased monotonically from 0.83 at 50 µS cm^{-1} to 0.55 at 800 µS cm^{-1} (Figure 6). Although the negative correlation between ε_{SP2} and κ was still present, $\varepsilon_{SP2\text{-}Ymax}$ was systematically (10% on average) higher than $\varepsilon_{SP2\text{-}Tin}$ across the full salinity range (κ>0 µS cm^{-1}). The size-dependent efficiency shown in Figure 7c indicates that the higher laser power did not improve the detection efficiency in the 70-100 nm D_{rBC} range. An improvement of $\varepsilon_{SP2\text{-}Ymax}$ was observed for rBC particles with D_{rBC} larger than 100-150 nm compared $\varepsilon_{SP2\text{-}Tin}$. It is evident that operating the pump laser at the maximum performance we could achieve does not impact the overall decreasing trend of ε_{SP2} with κ, and does not ensure homogeneous size detection of rBC particles in the typical SP2 size range. These results are consistent with quenching of incandescence due to coatings, with stronger reductions in smaller and more thickly-coated rBC cores, and explains the size shift observed in the snow samples, where the $GD_{rBC\text{-}M}$ increases by approximately 14% from S1 to S5 samples (Table 1). A similar increase was observed in the laboratory test (SP2 operated at maximum YAG-laser power) where $GD_{rBC\text{-}M}$ increases from 183 nm at~0 µS cm^{-1} to 211 nm at 800 µS cm^{-1} (15% increase). This similarity suggests that incandescence quenching might have completely masked the diameter increase caused by particles agglomeration during melting-freezing cycles that may have existed in the snow samples (Schwarz et al., 2012; Kinase et al., 2020). Diluting these samples to electrical conductivity values below 50 µS cm^{-1} (salt concentration of 0.03 g l^{-1}), when ε_{SP2} is higher than 80%, might significantly reduce incandescence quenching. However, the dilution factor will linearly increase with conductivity up to a factor of 16 for very saline samples (κ=800 µS cm^{-1}). Considering the low BC concentration generally observed in Arctic snow, dilution will strongly increase analysis time.

4 Conclusions

Laboratory experiments were conducted to assess the interference caused by inorganic salt on SP2 quantification of rBC mass and size distribution in saline snow samples nebulized with a Marin-5. These experiments were designed to reproduce the salinity conditions of snow samples collected over the sea ice-covered Fram Strait in summer 2017 during the PASCAL drift shipborne campaign. Such salt concentrations might be exclusively encountered in snow collected in coastal areas or over sea ice in the vicinity of open water. The total mass quantification efficiency (ε), which consists of the nebulization efficiency (ε_{Neb}) and the SP2 detection efficiency (ε_{SP2}), was strongly influenced by the salinity of fullerene suspension. Compared to ε of 0.58-0.66 for a non-saline fullerene soot suspension, high salinity (electrical conductivity of 800 μS cm^{-1} and NaCl concentration of 0.4 g l^{-1}) caused ε drop to 0.2-0.3. The sensitivity of ε_{SP2} to different SP2 settings was also tested to verify: 1) the impact of high number concentration of non-rBC particles on the SP2 signal acquisition; 2) the incandescence quenching produced by thick coatings. Different SP2 settings were tested, but none of them allowed unbiased detection of rBC mass, with maximum ε_{SP2} of approximately 0.85 and 0.55 for low- and high- saline samples; respectively. The SP2 detection efficiency was also found to strongly depend on the rBC core diameter. Overall, rBC cores below 100 nm were substantially undetected, showing ε_{SP2} below 0.2 for the most saline samples (electrical conductivity of 800 μS cm^{-1} and NaCl concentration of 0.4 g l^{-1}) compared to values above 0.6 for rBC particles larger than 200 nm. As a consequence of these interactions, the measured rBC mass concentration in the PASCAL snow samples was affected by a high degree of uncertainty and significantly biased low depending on snow salinity. By operating the SP2 in its optimal triggering setup and maximum YAG-laser power, the rBC mass concentrations in the less saline samples, collected after melting (electrical conductivity below 50 μS cm^{-1}) and representing 55% of total probes, the bias was limited to a maximum of 17%. In the most saline samples collected before melting (electrical conductivity above 800 μS cm^{-1} and NaCl concentration above 0.4 g l^{-1}) the measured rBC mass concentrations might have been biased low by at least by 45%. Note that the nebulization and sampling of saline samples might damage the SP2 directly, as well as affect its performance. Extremely saline samples can cause a temporary drop of the YAG-laser output power, and prolonged sampling of even low salinity samples can clog the SP2 internal airflow tubing. All told, these effects, when unrecognized and uncorrected, can alter the interpretation of natural processes. The work demonstrates the influences of sea salt on the performances of the SP2 system during the analysis of snow samples containing a notable amount of inorganic salt. This technical analytical issue has never been explicitly addressed beforehand and should be considered in the analysis of future studies conducted in marine regions. Additional work needs to be performed to minimize the impact of the matrix effect and to address the potential interference of salt on other BC measuring techniques.

Author contributions

MZ collected the snow samples and performed the SP2, SMPS, and physical measurements. OE performed the ALBAMA measurements. AH, ZJ, JPS contributed to the SP2 data interpretation. JS contributed to the ALABAMA data interpretation. MZ drafted the paper with contributions from all co-authors.

Competing interests
The authors declare that they have no conflict of interest.

Special issue statement. This article is part of the special issue "Arctic mixed-phase clouds as studied during the ACLOUD/PASCAL campaigns in the framework of (AC)3 (ACP/AMT/ESSD inter-journal SI)". It is not associated with a conference.

Acknowledgements: We gratefully acknowledge the funding by the Deutsche Forschungsgemeinschaft (DFG, German Research Foundation)– project ID 268020496 – TRR 172, within the Transregional Collaborative Research Center "ArctiC Amplification: Climate Relevant Atmospheric and SurfaCe Processes, and Feedback Mechanisms (AC)3". OE acknowledges funding by the Max Planck Graduate School (MPGC).

References

Baumgardner, D., Popovicheva, O., Allan, J., Bernardoni, V., Cao, J., Cavalli, F., Cozic, J., Diapouli, E., Eleftheriadis, K., Genberg, P. J., Gonzalez, C., Gysel, M., John, A., Kirchstetter, T. W., Kuhlbusch, T. A. J., Laborde, M., Lack, D., Müller, T., Niessner, R., Petzold, A., Piazzalunga, A., Putaud, J. P., Schwarz, J., Sheridan, P., Subramanian, R., Swietlicki, E., Valli, G., Vecchi, R., and Viana, M.: Soot reference materials for instrument calibration and intercomparisons: a workshop summary with recommendations, Atmos Meas Tech, 5, 1869–1887, https://doi.org/10.5194/amt-5-1869-2012, 2012.

Brands, M., Kamphus, M., Böttger, T., Schneider, J., Drewnick, F., Roth, A., Curtius, J., Voigt, C., Borbon, A., Beekmann, M., Bourdon, A., Perrin, T., and Borrmann, S.: Characterization of a Newly Developed Aircraft-Based Laser Ablation Aerosol Mass Spectrometer (ALABAMA) and First Field Deployment in Urban Pollution Plumes over Paris During MEGAPOLI 2009, Aerosol Sci. Technol., 45, 46–64, https://doi.org/10.1080/02786826.2010.517813, 2011.

Burgener, J. A. and Makonnen, Y.: Chapter 2 - Nebulization systems, in: Sample Introduction Systems in ICPMS and ICPOES, edited by: Beauchemin, D., Elsevier, Amsterdam, 57–142, https://doi.org/10.1016/B978-0-444-59482-2.00002-6, 2020.

Cano, J. M., Todolí, J. L., Hernandis, V., and Mora, J.: The role of the nebulizer on the sodium interferent effects in inductively coupled plasma atomic emission spectrometry, J Anal Spectrom, 17, 57–63, https://doi.org/10.1039/B105077J, 2002.

Clarke, A. D. and Noone, K. J.: Soot in the Arctic snowpack: a cause for perturbations in radiative transfer, Atmospheric Environ. 1967, 19, 2045–2053, https://doi.org/10.1016/0004-6981(85)90113-1, 1985.

Clemen, H.-C., Schneider, J., Klimach, T., Helleis, F., Köllner, F., Hünig, A., Rubach, F., Mertes, S., Wex, H., Stratmann, F., Welti, A., Kohl, R., Frank, F., and Borrmann, S.: Optimizing the detection, ablation, and ion extraction efficiency of a single-particle laser ablation mass spectrometer for application in environments with low aerosol particle concentrations, Atmospheric Meas. Tech., 13, 5923–5953, https://doi.org/10.5194/amt-13-5923-2020, 2020.

Clifford, R. H., Tan, H., Liu, H., Montaser, A., Zarrin, F., and Keady, P. B.: Particle size measurements in the submicron range by the differential electromobility technique: comparison of aerosols from thermospray, ultrasonic, pneumatic and frit-type nebulizers, Spectrochim. Acta Part B At. Spectrosc., 48, 1221–1235, https://doi.org/10.1016/0584-8547(93)80107-6, 1993.

Doherty, S. J., Warren, S. G., Grenfell, T. C., Clarke, A. D., and Brandt, R. E.: Light-absorbing impurities in Arctic snow, Atmospheric Chem. Phys., 10, 11647–11680, https://doi.org/10.5194/acp-10-11647-2010, 2010.

Doherty, S. J., Grenfell, T. C., Forsström, S., Hegg, D. L., Brandt, R. E., and Warren, S. G.: Observed vertical redistribution of black carbon and other insoluble light-absorbing particles in melting snow, J. Geophys. Res. Atmospheres, 118, 5553–5569, https://doi.org/10.1002/jgrd.50235, 2013.

Domine, F., Sparapani, R., Ianniello, A., and Beine, H. J.: The origin of sea salt in snow on Arctic sea ice and in coastal regions, Atmospheric Chem. Phys., 4, 2259–2271, https://doi.org/10.5194/acp-4-2259-2004, 2004.

Domine, F., Taillandier, A.-S., and Simpson, W. R.: A parameterization of the specific surface area of seasonal snow for field use and for models of snowpack evolution, J. Geophys. Res. Earth Surf., 112, https://doi.org/10.1029/2006JF000512, 2007.

Dou, T.-F. and Xiao, C.-D.: An overview of black carbon deposition and its radiative forcing over the Arctic, Adv. Clim. Change Res., 7, 115–122, https://doi.org/10.1016/j.accre.2016.10.003, 2016.

Dubuisson, C., Poussel, E., and Mermet, J. M.: Comparison of ionic line-based internal standardization with axially and radially viewed inductively coupled plasma atomic emission spectrometry to compensate for sodium effects on accuracy, J. Anal. At. Spectrom., 13, 1265–1269, https://doi.org/10.1039/A805424J, 1998.

Flanner, M. G., Zender, C. S., Randerson, J. T., and Rasch, P. J.: Present-day climate forcing and response from black carbon in snow, J. Geophys. Res. Atmospheres, 112, D11202, https://doi.org/10.1029/2006JD008003, 2007.

Flores, H. and Macke, A.: The Expeditions PS106/1 and 2 of the Research Vessel POLARSTERN to the Arctic Ocean in 2017, Alfred-Wegener-Institut, Helmholtz-Zentrum für Polar- und Meeresforschung, https://doi.org/10.2312/BZPM_0719_2018, 2018.

Gysel, M., Laborde, M., Olfert, J. S., Subramanian, R., and Gröhn, A. J.: Effective density of Aquadag and fullerene soot black carbon reference materials used for SP2 calibration, Atmos Meas Tech, 4, 2851–2858, https://doi.org/10.5194/amt-4-2851-2011, 2011.

Haas, C., Thomas, D. N., and Bareiss, J.: Surface properties and processes of perennial Antarctic sea ice in summer, J. Glaciol., 47, 613–625, https://doi.org/10.3189/172756501781831864, 2001.

Hagler, G. S. W., Bergin, M. H., Smith, E. A., Dibb, J. E., Anderson, C., and Steig, E. J.: Particulate and water-soluble carbon measured in recent snow at Summit, Greenland, Geophys. Res. Lett., 34, https://doi.org/10.1029/2007GL030110, 2007.

Hansen, J. and Nazarenko, L.: Soot climate forcing via snow and ice albedos, Proc. Natl. Acad. Sci., 101, 423–428, https://doi.org/10.1073/pnas.2237157100, 2004.

Hayashi, M.: Temperature-Electrical Conductivity Relation of Water for Environmental Monitoring and Geophysical Data Inversion, Environ. Monit. Assess., 96, 119–128, https://doi.org/10.1023/B:EMAS.0000031719.83065.68, 2004.

Jacobi, H.-W., Obleitner, F., Costa, S. D., Ginot, P., Eleftheriadis, K., Aas, W., and Zanatta, M.: Deposition of ionic species and black carbon to the Arctic snowpack: combining snow pit observations with modeling, Atmospheric Chem. Phys., 19, 10361–10377, https://doi.org/10.5194/acp-19-10361-2019, 2019.

Katich, J. M., Perring, A. E., and Schwarz, J. P.: Optimized detection of particulates from liquid samples in the aerosol phase: Focus on black carbon, Aerosol Sci. Technol., 51, 543–553, https://doi.org/10.1080/02786826.2017.1280597, 2017.

Khan, A. L., Dierssen, H., Schwarz, J. P., Schmitt, C., Chlus, A., Hermanson, M., Painter, T. H., and McKnight, D. M.: Impacts of coal dust from an active mine on the spectral reflectance of Arctic surface snow in Svalbard, Norway, J. Geophys. Res. Atmospheres, 122, 1767–1778, https://doi.org/10.1002/2016JD025757, 2017.

Kinase, T., Adachi, K., Oshima, N., Goto-Azuma, K., Ogawa-Tsukagawa, Y., Kondo, Y., Moteki, N., Ohata, S., Mori, T., Hayashi, M., Hara, K., Kawashima, H., and Kita, K.: Concentrations and Size Distributions of Black Carbon in the Surface Snow of Eastern Antarctica in 2011, J. Geophys. Res. Atmospheres, 125, e2019JD030737, https://doi.org/10.1029/2019JD030737, 2020.

Köllner, F., Schneider, J., Willis, M. D., Klimach, T., Helleis, F., Bozem, H., Kunkel, D., Hoor, P., Burkart, J., Leaitch, W. R., Aliabadi, A. A., Abbatt, J. P. D., Herber, A. B., and Borrmann, S.: Particulate trimethylamine in the summertime Canadian high Arctic lower troposphere, Atmospheric Chem. Phys., 17, 13747–13766, https://doi.org/10.5194/acp-17-13747-2017, 2017.

Krnavek, L., Simpson, W. R., Carlson, D., Domine, F., Douglas, T. A., and Sturm, M.: The chemical composition of surface snow in the Arctic: Examining marine, terrestrial, and atmospheric influences, Atmos. Environ., 50, 349–359, https://doi.org/10.1016/j.atmosenv.2011.11.033, 2012.

Laborde, M., Mertes, P., Zieger, P., Dommen, J., Baltensperger, U., and Gysel, M.: Sensitivity of the Single Particle Soot Photometer to different black carbon types, Atmos Meas Tech, 5, 1031–1043, https://doi.org/10.5194/amt-5-1031-2012, 2012a.

Laborde, M., Schnaiter, M., Linke, C., Saathoff, H., Naumann, K.-H., Möhler, O., Berlenz, S., Wagner, U., Taylor, J. W., Liu, D., Flynn, M., Allan, J. D., Coe, H., Heimerl, K., Dahlkötter, F., Weinzierl, B., Wollny, A. G., Zanatta, M., Cozic, J., Laj, P., Hitzenberger, R., Schwarz, J. P., and Gysel, M.: Single Particle Soot Photometer intercomparison at the AIDA chamber, Atmospheric Meas. Tech., 5, 3077–3097, https://doi.org/10.5194/amt-5-3077-2012, 2012b.

Lide, D. R.: CRC Handbook of Chemistry and Physics: A Ready-reference Book of Chemical and Physical Data, CRC Press, 2648 pp., 1995.

Lim, S., Faïn, X., Zanatta, M., Cozic, J., Jaffrezo, J.-L., Ginot, P., and Laj, P.: Refractory black carbon mass concentrations in snow and ice: method evaluation and inter-comparison with elemental carbon measurement, Atmos Meas Tech, 7, 3307–3324, https://doi.org/10.5194/amt-7-3307-2014, 2014.

L. Sharp, B.: Pneumatic nebulisers and spray chambers for inductively coupled plasma spectrometry. A review. Part 1. Nebulisers, J. Anal. At. Spectrom., 3, 613–652, https://doi.org/10.1039/JA9880300613, 1988.

Luis Todolí, J., Gras, L., Hernandis, V., and Mora, J.: Elemental matrix effects in ICP-AES, J. Anal. At. Spectrom., 17, 142–169, https://doi.org/10.1039/B009570M, 2002.

Macdonald, K. M., Sharma, S., Toom, D., Chivulescu, A., Hanna, S., Bertram, A. K., Platt, A., Elsasser, M., Huang, L., Tarasick, D., Chellman, N., McConnell, J. R., Bozem, H., Kunkel, D., Lei, Y. D., Evans, G. J., and Abbatt, J. P. D.: Observations of atmospheric chemical deposition to high Arctic snow, Atmospheric Chem. Phys., 17, 5775–5788, https://doi.org/10.5194/acp-17-5775-2017, 2017.

Massom, R. A., Eicken, H., Hass, C., Jeffries, M. O., Drinkwater, M. R., Sturm, M., Worby, A. P., Wu, X., Lytle, V. I., Ushio, S., Morris, K., Reid, P. A., Warren, S. G., and Allison, I.: Snow on Antarctic sea ice, Rev. Geophys., 39, 413–445, https://doi.org/10.1029/2000RG000085, 2001.

Mori, T., Moteki, N., Ohata, S., Koike, M., Goto-Azuma, K., Miyazaki, Y., and Kondo, Y.: Improved technique for measuring the size distribution of black carbon particles in liquid water, Aerosol Sci. Technol., 50, 242–254, https://doi.org/10.1080/02786826.2016.1147644, 2016.

Mori, T., Goto-Azuma, K., Kondo, Y., Ogawa-Tsukagawa, Y., Miura, K., Hirabayashi, M., Oshima, N., Koike, M., Kupiainen, K., Moteki, N., Ohata, S., Sinha, P. R., Sugiura, K., Aoki, T., Schneebeli, M., Steffen, K., Sato, A., Tsushima, A., Makarov, V., Omiya, S., Sugimoto, A., Takano, S., and Nagatsuka, N.: Black Carbon and Inorganic Aerosols in Arctic Snowpack, J. Geophys. Res. Atmospheres, 124, 13325–13356, https://doi.org/10.1029/2019JD030623, 2019.

Mori, T., Kondo, Y., Ohata, S., Zhao, Y., Sinha, P. R., Oshima, N., Matsui, H., Moteki, N., and Koike, M.: Seasonal Variation of Wet Deposition of Black Carbon in Arctic Alaska, J. Geophys. Res. Atmospheres, 125, e2019JD032240, https://doi.org/10.1029/2019JD032240, 2020.

Moteki, N. and Kondo, Y.: Dependence of Laser-Induced Incandescence on Physical Properties of Black Carbon Aerosols: Measurements and Theoretical Interpretation, Aerosol Sci. Technol., 44, 663–675, https://doi.org/10.1080/02786826.2010.484450, 2010.

Olivares, J. A. and Houk, R. S.: Suppression of analyte signal by various concomitant salts in inductively coupled plasma mass spectrometry, Anal Chem U. S., 58:1, https://doi.org/10.1021/ac00292a008, 1986.

Ozdemir, O., Karakashev, S. I., Nguyen, A. V., and Miller, J. D.: Adsorption and surface tension analysis of concentrated alkali halide brine solutions, Miner. Eng., 22, 263–271, https://doi.org/10.1016/j.mineng.2008.08.001, 2009.

Petzold, A., Ogren, J. A., Fiebig, M., Laj, P., Li, S.-M., Baltensperger, U., Holzer-Popp, T., Kinne, S., Pappalardo, G., Sugimoto, N., Wehrli, C., Wiedensohler, A., and Zhang, X.-Y.: Recommendations for reporting "black carbon" measurements, Atmos Chem Phys, 13, 8365–8379, https://doi.org/10.5194/acp-13-8365-2013, 2013.

Quinn, P. K., Stohl, A., Arnold, S., Baklanov, A., Berntsen, T. K., Christensen, J. H., Eckhardt, S., Flanner, M., Klimont, Z., Korsholm, U. S., and others: AMAP Assessment 2015: Black carbon and ozone as Arctic climate forcers, 2015.

Rösch, M. and Cziczo, D. J.: Aqueous particle generation with a 3D printed nebulizer, Aerosols/Laboratory Measurement/Instruments and Platforms, https://doi.org/10.5194/amt-2020-155, 2020.

Schacht, J., Heinold, B., Quaas, J., Backman, J., Cherian, R., Ehrlich, A., Herber, A., Huang, W. T. K., Kondo, Y., Massling, A., Sinha, P. R., Weinzierl, B., Zanatta, M., and Tegen, I.: The importance of the representation of air pollution emissions for the modeled distribution and radiative effects of black carbon in the Arctic, Atmospheric Chem. Phys., 19, 11159–11183, https://doi.org/10.5194/acp-19-11159-2019, 2019.

Schnaiter, M., Linke, C., Ibrahim, I., Kiselev, A., Waitz, F., Leisner, T., Norra, S., and Rehm, T.: Specifying the light-absorbing properties of aerosol particles in fresh snow samples, collected at the Environmental Research Station Schneefernerhaus (UFS), Zugspitze, Atmospheric Chem. Phys., 19, 10829–10844, https://doi.org/10.5194/acp-19-10829-2019, 2019.

Schwarz, J. P., Spackman, J. R., Gao, R. S., Perring, A. E., Cross, E., Onasch, T. B., Ahern, A., Wrobel, W., Davidovits, P., Olfert, J., Dubey, M. K., Mazzoleni, C., and Fahey, D. W.: The Detection Efficiency of the Single Particle Soot Photometer, Aerosol Sci. Technol., 44, 612–628, https://doi.org/10.1080/02786826.2010.481298, 2010.

Schwarz, J. P., Doherty, S. J., Li, F., Ruggiero, S. T., Tanner, C. E., Perring, A. E., Gao, R. S., and Fahey, D. W.: Assessing Single Particle Soot Photometer and Integrating Sphere/Integrating Sandwich Spectrophotometer measurement techniques for quantifying black carbon concentration in snow, Atmos Meas Tech, 5, 2581–2592, https://doi.org/10.5194/amt-5-2581-2012, 2012.

Sinha P. R., Kondo Y., Goto-Azuma K., Tsukagawa Y., Fukuda K., Koike M., Ohata S., Moteki N., Mori T., Oshima N., Førland E. J., Irwin M., Gallet J.-C., and Pedersen C. A.: Seasonal Progression of the Deposition of Black Carbon by Snowfall at Ny-Ålesund, Spitsbergen, J. Geophys. Res. Atmospheres, 123, 997–1016, https://doi.org/10.1002/2017JD028027, 2017.

Skiles, S. M. and Painter, T.: Daily evolution in dust and black carbon content, snow grain size, and snow albedo during snowmelt, Rocky Mountains, Colorado, J. Glaciol., 63, 118–132, https://doi.org/10.1017/jog.2016.125, 2017.

Skiles, S. M., Flanner, M., Cook, J. M., Dumont, M., and Painter, T. H.: Radiative forcing by light-absorbing particles in snow, Nat. Clim. Change, 8, 964–971, https://doi.org/10.1038/s41558-018-0296-5, 2018.

Sötebier, C., Kutscher, D., Rottmann, L., Jakubowski, N., Panne, U., and Bettmer, J.: Combination of single particle ICP-QMS and isotope dilution analysis for the determination of size, particle number and number size distribution of silver nanoparticles, J. Anal. At. Spectrom., 31, 2045–2052, https://doi.org/10.1039/C6JA00137H, 2016.

Tørseth, K.: Review of Observation Capacities and Data Availability for Black Carbon in the Arctic Region:EU Action on Black Carbon inthe Arctic – Technical Report 1, 2019.

von der Weiden, S.-L., Drewnick, F., and Borrmann, S.: Particle Loss Calculator – a new software tool for the assessment of the performance of aerosol inlet systems, Atmos Meas Tech, 2, 479–494, https://doi.org/10.5194/amt-2-479-2009, 2009.

Wendisch, M., Macke, A., Ehrlich, A., Lüpkes, C., Mech, M., Chechin, D., Dethloff, K., Velasco, C. B., Bozem, H., Brückner, M., Clemen, H.-C., Crewell, S., Donth, T., Dupuy, R., Ebell, K., Egerer, U., Engelmann, R., Engler, C., Eppers, O., Gehrmann, M., Gong, X., Gottschalk, M., Gourbeyre, C., Griesche, H., Hartmann, J., Hartmann, M., Heinold, B., Herber, A., Herrmann, H., Heygster, G., Hoor, P., Jafariserajehlou, S., Jäkel, E., Järvinen, E., Jourdan, O., Kästner, U., Kecorius, S., Knudsen, E. M., Köllner, F., Kretzschmar, J., Lelli, L., Leroy, D., Maturilli, M., Mei, L., Mertes, S., Mioche, G., Neuber, R., Nicolaus, M., Nomokonova, T., Notholt, J., Palm, M., van Pinxteren, M., Quaas, J., Richter, P., Ruiz-Donoso, E., Schäfer, M., Schmieder, K., Schnaiter, M., Schneider, J., Schwarzenböck, A., Seifert, P., Shupe, M. D., Siebert, H., Spreen, G., Stapf, J., Stratmann, F., Vogl, T., Welti, A., Wex, H., Wiedensohler, A., Zanatta, M., and Zeppenfeld, S.: The Arctic Cloud Puzzle: Using ACLOUD/PASCAL Multiplatform Observations to Unravel the Role of Clouds and Aerosol Particles in Arctic Amplification, Bull. Am. Meteorol. Soc., 100, 841–871, https://doi.org/10.1175/BAMS-D-18-0072.1, 2018.

Wendl, I. A., Menking, J. A., Färber, R., Gysel, M., Kaspari, S. D., Laborde, M. J. G., and Schwikowski, M.: Optimized method for black carbon analysis in ice and snow using the Single Particle Soot Photometer, Atmos Meas Tech, 7, 2667–2681, https://doi.org/10.5194/amt-7-2667-2014, 2014.

Zhang, Y., Kang, S., Gao, T., Sprenger, M., Dou, T., Han, W., Zhang, Q., Sun, S., Du, W., Chen, P., Guo, J., Cui, X., and Sillanpää, M.: Dissolved organic carbon in Alaskan Arctic snow: concentrations, light-absorption properties, and bioavailability, Tellus B Chem. Phys. Meteorol., 72, 1–19, https://doi.org/10.1080/16000889.2020.1778968, 2020.

Tables

Table 1 Properties of snow samples grouped in conductivity classes. Conductivity of melted samples measured between 20 and 25 °C. Total aerosolized particles measured in the mobility diameter range 14-685 nm: number concentration (N), geometric mean of the number size distribution ($GD_{P\text{-}N}$). rBC particles measured between 60 and 1000 nm of D_{rBC}: number concentration (N_{rBC}), mass mixing ratio (M_{rBC}), geometric mean of the number ($GD_{rBC\text{-}N}$) and mass ($GD_{rBC\text{-}M}$) size distribution. Number fraction of rBC particles (F_{rBC}).

Salinity class	Fraction sample [%]	Conductivity [µS cm^{-1}]			N [cm^{-3}]		$GD_{P\text{-}N}$ [nm]	N_{rBC} [cm^{-3}]		GD_{rBC} [nm]	F_{rBC} [%]	M_{rBC} [ng g^{-1}]		$GD_{rBC\text{-}M}$ [nm]
		Min	Max	Mean	Mean	SD		Mean	SD		Mean	Mean	SD	
S1	38	5.3	10.3	7.07	$6.1*10^5$	$1.3*10^5$	27.3	69.6	34.04	87.6	$1.1*10^{-2}$	8.05	4.29	225
S2	17	19.6	33.1	24.9	$9.5*10^5$	$1.0*10^5$	34.4	13.1	1.64	89.2	$1.4*10^{-3}$	1.57	0.41	229
S3	21	219	343	266	$1.3*10^6$	$6.2*10^4$	57.6	6.81	2.03	94.2	$5.2*10^{-4}$	0.66	0.21	212
S4	13	466	533	497	$1.4*10^6$	$6.7*10^4$	72.1	4.45	3.71	106	$3.1*10^{-4}$	0.56	0.44	246
S5	13	1275	1652	1424	$1.5*10^6$	$9.0*10^4$	89.0	1.71	0.26	120	$1.1*10^{-4}$	0.27	0.12	257

Figures

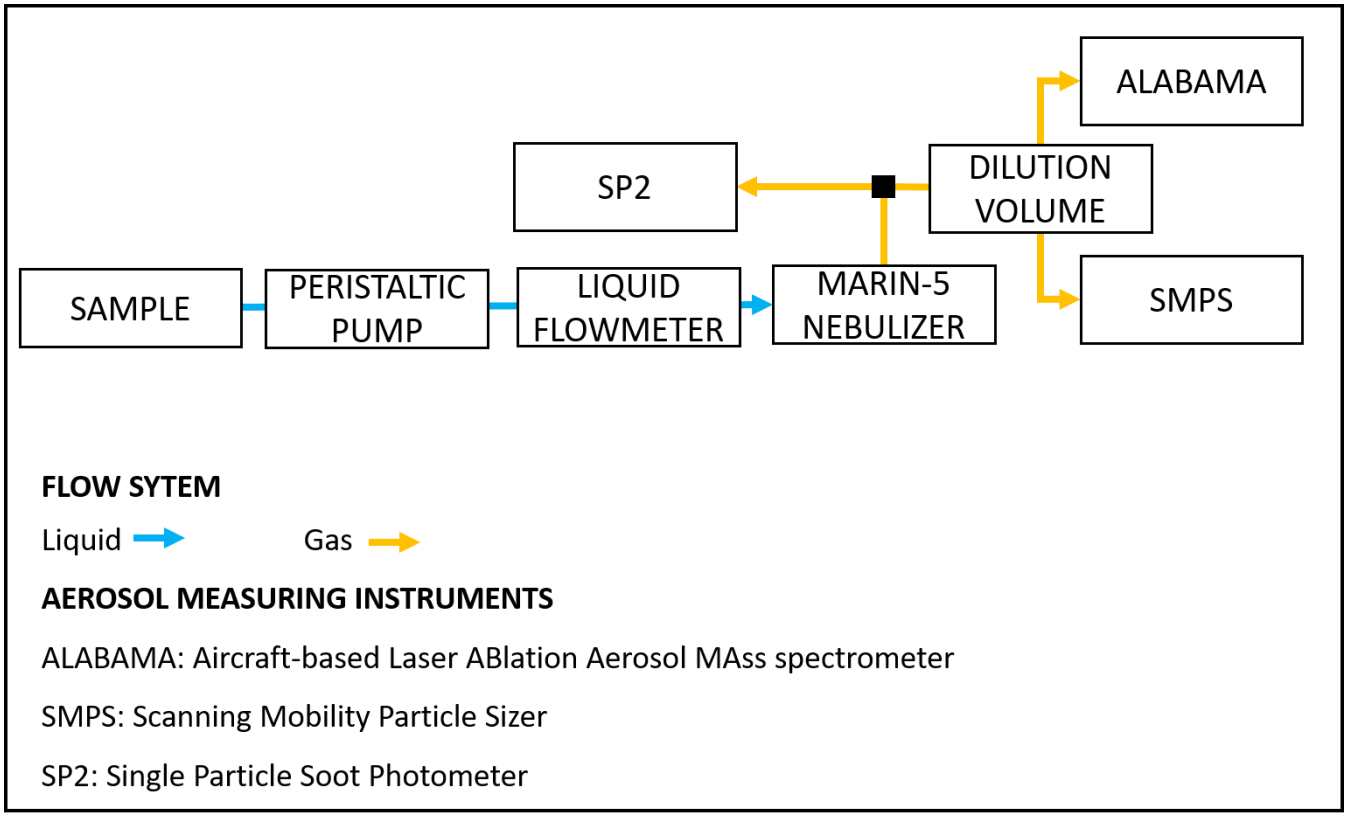

790 **Figure 1 Schematics of the instrumental setup deployed to analyze the PASCAL snow samples and to perform the laboratory test experiments. ALABAMA not available for laboratory test experiments.**

795

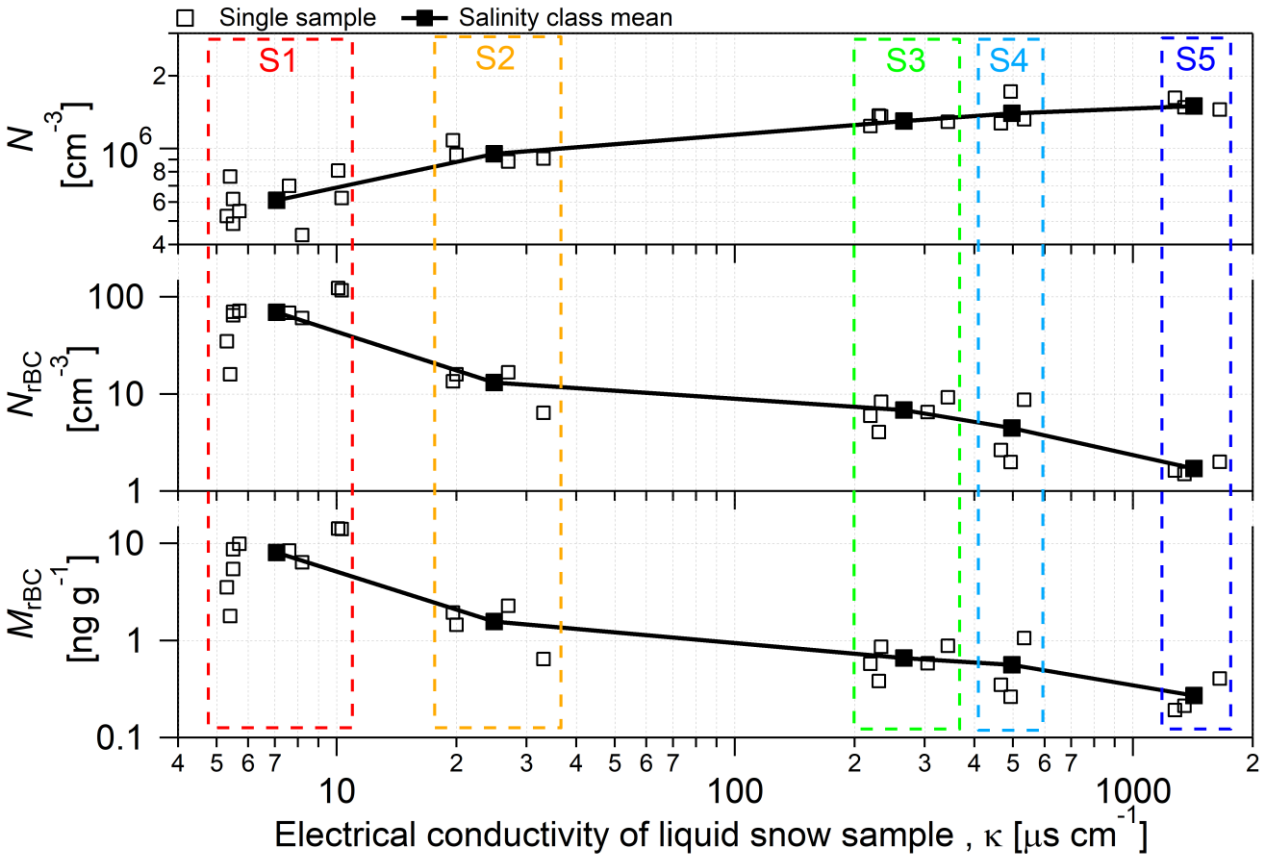

Figure 2 a) Number concentration of the total particles (*N*), b) number concentration rBC particles (N_{rBC}) and c) mass mixing ratio (M_{rBC}) produced from the nebulization of PASCAL snow samples as a function of the electrical conductivity of melted snow samples. Boxes indicate the salinity classes (Sn). *N* measured with the SPMS in the 14-680 nm diameter range nm. rBC particles measure with the SP2 in the 70-1000 nm diameter range. S1, S2, S3, S4, S5 represent the salinity classes.

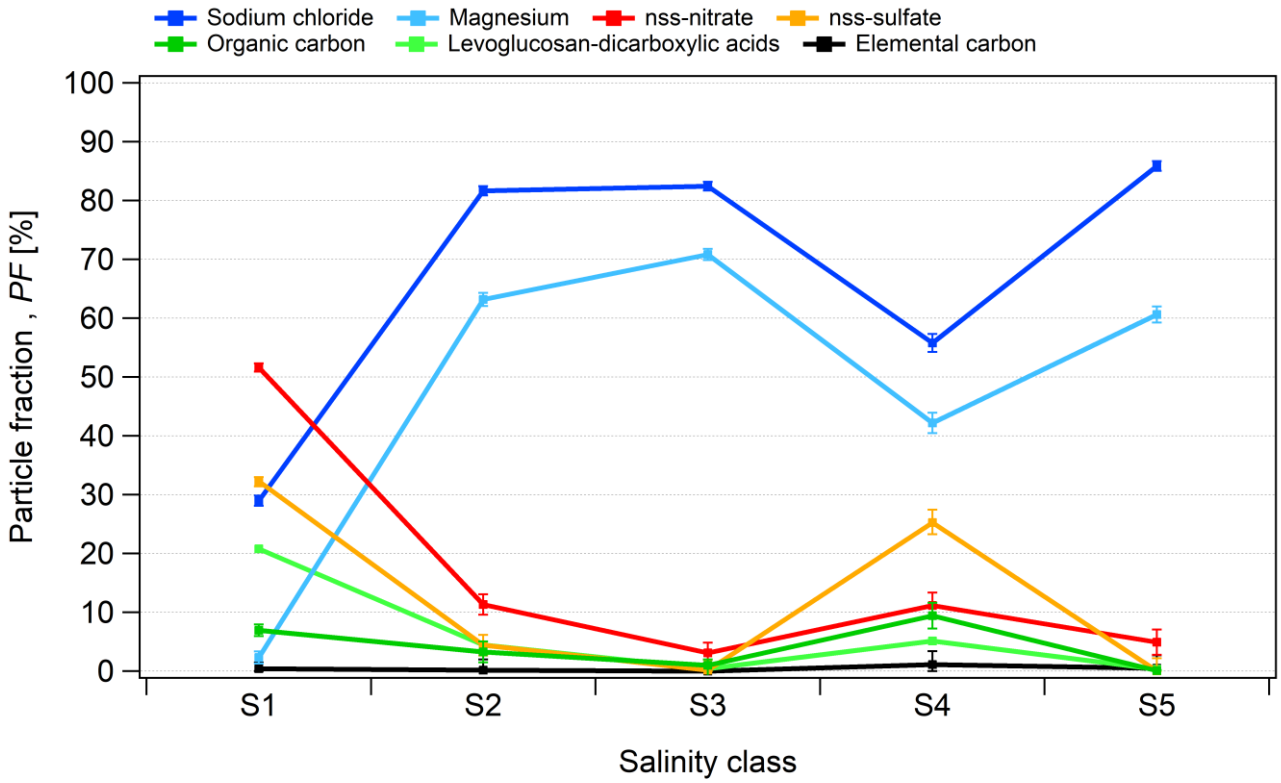

805 **Figure 3 Number fraction of analyzed particles (*PF*) containing given chemical species measured by ALABAMA in the PASCAL snow samples as a function of the salinity classes (Sn). The selected species: sodium chloride (NaCl), non-sea-salt (nss) nitrate, nss sulfate, magnesium (Mg), levoglucosan and dicarboxylic acids, organic carbon (OC) and elemental carbon (EC). Chemical composition measured for particles in the 110-5000 nm diameter range.**

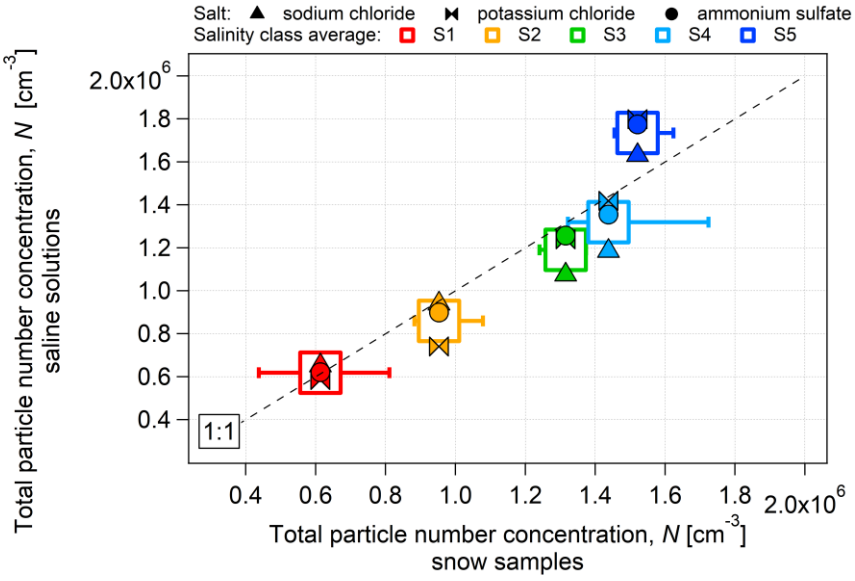

Figure 4 Comparison of number concentration of aerosolized particles produced from inorganic salt solutions (sodium chloride, potassium chloride, ammonium sulfate) and snow samples as a function of salinity.

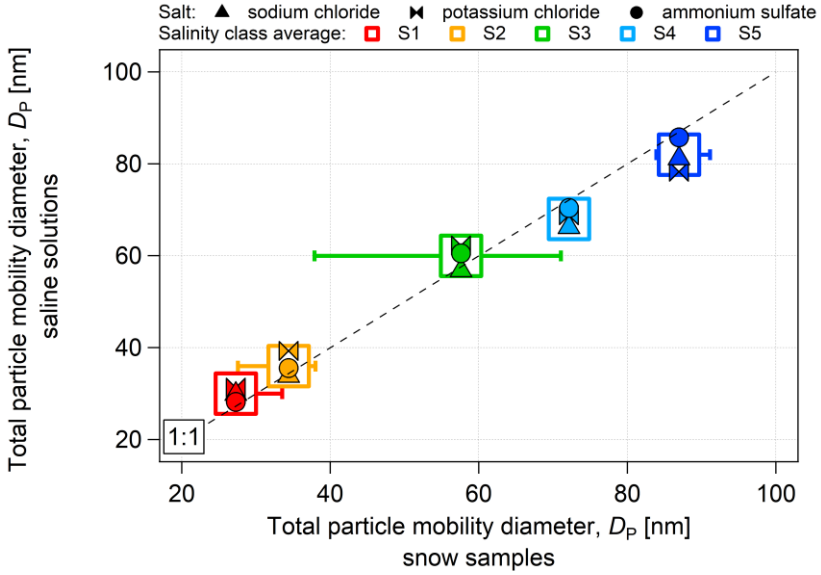

Figure 5 Comparison of diameter of aerosolized particles produced from inorganic salt solutions (sodium chloride, potassium chloride, ammonium sulfate) and snow samples as a function of salinity. Diameter expressed as geometric mean diameter calculated from the number size distribution of aerosolized particles.

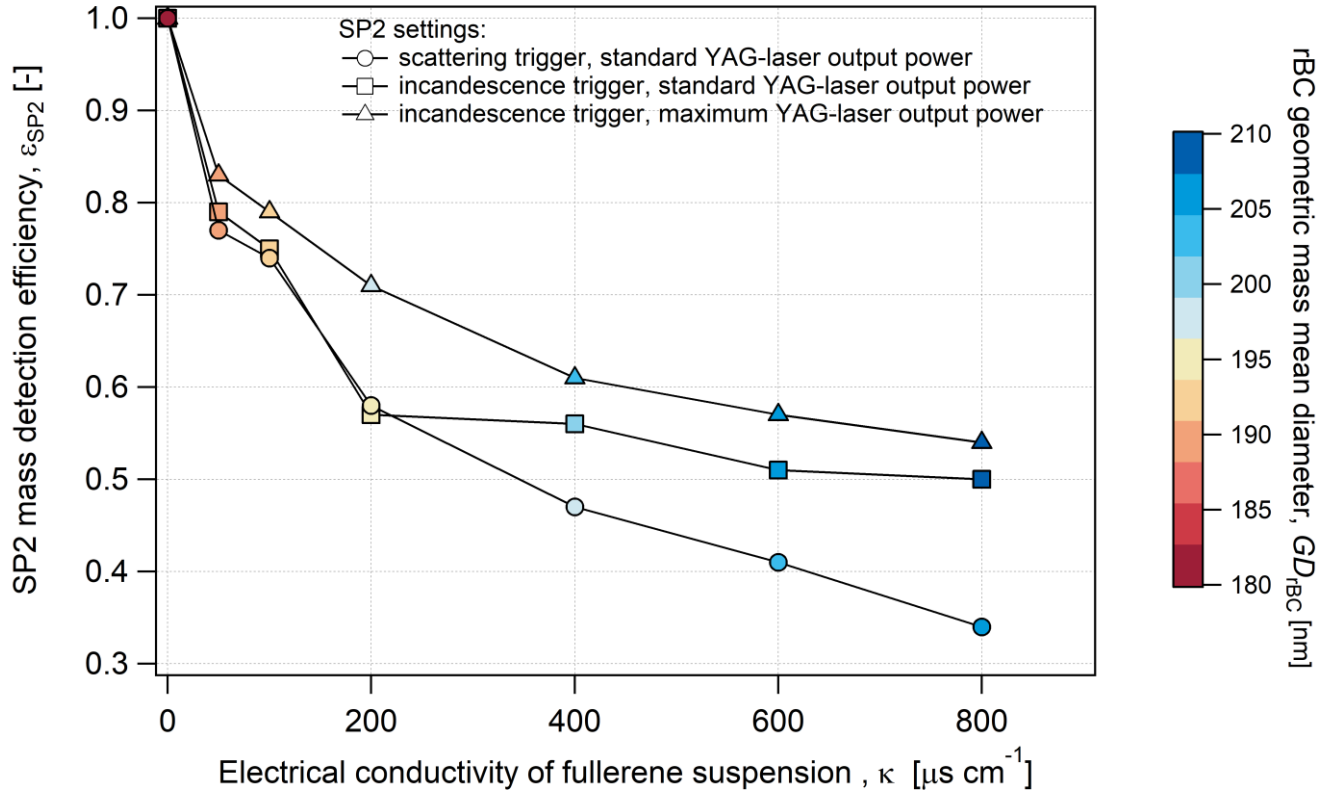

825

Figure 6 Mass detection efficiency of the SP2 for different SP2 settings and increasing electrical conductivity. Data acquired from the analysis of a fullerene soot suspension at 10 µg l^{-1}.

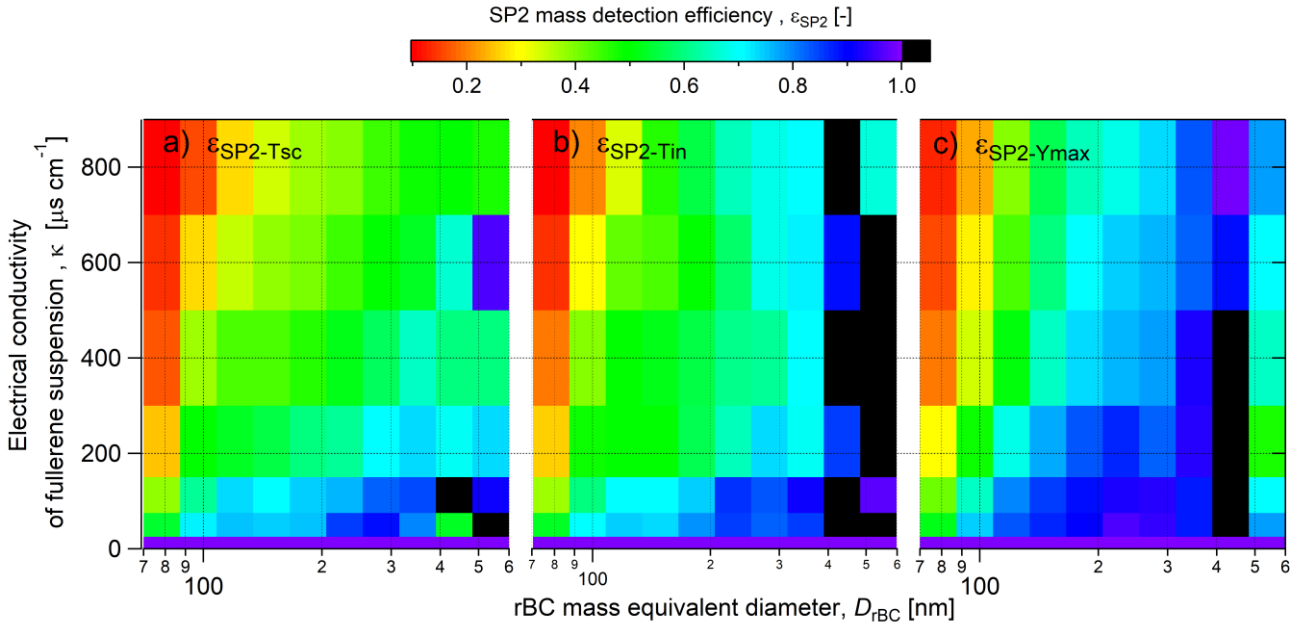

Figure 7 rBC mass detection efficiency as a function of D_{rBC} for different SP2 settings. a) acquisition triggered on the scattering detector with standard YAG-laser output power, $\varepsilon_{SP2\text{-}Tsc}$; b) acquisition triggered on the incandescence detector with standard YAG-laser output power $\varepsilon_{SP2\text{-}Tin}$; c) acquisition triggered on the incandescence detector with maximum YAG-laser output power, $\varepsilon_{SP2\text{-}Ymax}$. Results for fullerene soot suspensions with a concentration of 10 µg l^{-1}.